

Filling the gap: Enhancing borehole imaging with a tensor neural network

Dawei Liu¹, Qingfang Wang², Nan You³, Mauricio D. Sacchi⁴, and Wenchao Chen²

ABSTRACT

Borehole imaging is crucial in geologic research as it offers insights into subsurface formations and supports reservoir assessment, mineral exploration, and hydrocarbon extraction. However, the effectiveness of borehole imaging is limited by the incompleteness of data due to the design constraints of borehole imaging tools. Missing areas in borehole images pose challenges to geologists. Although existing methods, such as pattern filling and convolutional neural network-based techniques, show some efficacy, they often require a large number of complete images for training. In recent years, unsupervised deep-learning and tensor-based methods have gained attention for their ability to reconstruct missing or degraded geologic images by leveraging the structural characteristics of these images. In particular, tensor representations based on Tucker decomposition have shown strong capabilities in data completion.

Inspired by this, we develop a novel self-supervised tensor neural network (TNN) using Tucker decomposition as our backbone. Because borehole images are originally in 2D, converting them into tensor representations is a critical step in leveraging our tensor representation. To achieve this, we introduce the adaptive boundary-detection cropping with augmentation algorithm, which adapts 2D images into 3D tensors. After interpolating the tensors using our tensor network, we use adaptive slice concatenation with replacement to restore complete images from the enhanced tensors, ensuring that the tensor representation of the 3D data is accurately shown in 2D images. Our TNN can be further enhanced by incorporating a structural regularizer. Actual data experiments demonstrate that our method effectively fills gaps in borehole images with greater clarity and detail. The completed images retain the crucial geologic features and textures, surpassing some of the existing self-supervised learning methods.

INTRODUCTION

In geologic research, borehole microresistivity imaging is a pivotal tool, offering insights that enable a profound understanding of subsurface formations. This technology has facilitated the visualization of geologic structures and features, thereby aiding in the comprehension of reservoir properties, mineral exploration, and hydrocarbon extraction (Lofts and Bourke, 1999). This paper focuses on images obtained by the formation microscopic imager (FMI), which is crucial in advancing borehole imaging by providing high-resolution images of borehole walls (Rider, 1986; Luthi, 2001). These images, obtained by measuring microresistivity variations, reflect changes in fluid, rock, and structural characteristics

within subsurface formations, providing valuable information for geologic research. For example, the detailed information on rock properties provided by borehole images is crucial for reservoir assessment, enabling a deeper understanding of lithology, shale content, fluid distribution, and fractures.

However, one of the primary challenges faced by borehole imaging is the issue of data gaps resulting from the design limitations of the borehole imaging logging tools, which may lead to voids in the images. Although FMI borehole images achieve a coverage rate of 60%, the remaining 40% (Jiang et al., 2024) contains gaps, making the interpretation of the images more challenging and potentially leading to inaccuracies in estimating factors, such as fractures. Although introducing new logging tools or combinations

Manuscript received by the Editor 17 April 2024; revised manuscript received 27 October 2024; published ahead of production 26 December 2024.

¹Xi'an Jiaotong University, School of Information and Communications Engineering, Xi'an, China, and University of Alberta, Department of Physics, Edmonton, Alberta, Canada. E-mail: 409791715@qq.com.

²Xi'an Jiaotong University, School of Information and Communications Engineering, Xi'an, China. E-mail: wangqf010305@163.com; wencchen@xjtu.edu.cn (corresponding author).

³Aramco Americas, Houston Research Center, Houston, Texas, USA. E-mail: nan.you@aramcoamericas.com.

⁴University of Alberta, Department of Physics, Edmonton, Alberta, Canada. E-mail: msacchi@ualberta.ca.

© 2025 Society of Exploration Geophysicists. All rights reserved.

of tools can reduce these gaps, completely eliminating them during data collection remains a significant challenge.

Researchers have proposed various methods to address this issue, such as traditional pattern-filling and data-driven techniques. For example, Filtersim (Zhang et al., 2006; Mariethoz and Renard, 2010; Mustapha and Dimitrakopoulos, 2010; Hurley and Zhang, 2011) is a commonly used pattern-filling algorithm that fills gaps in formation images by extracting patterns from other image regions or databases. However, for complex geologic structures, such as large formations or elongated curves, Filtersim's filling effect often needs to be improved. To tackle this issue, some researchers have proposed advanced techniques based on multiple-point statistics (MPS) to reconstruct the missing parts of formation images better. Although these methods have achieved some success in some instances, they often require large amounts of complete image data as training samples. Compared with the MPS method, Assous et al. (2014) use the sparse representation of multiscale and multidirectional curvelet transforms to decompose the imaging sections into morphological components. The complete borehole image is then obtained through the inverse transformation and reconstruction of these components. This method does not require training data but encounters labor-intensive parameter selection.

With the rapid development of deep-learning technology, convolutional neural network (CNN)-based image inpainting methods have gained widespread attention, such as blind inpainting CNN (Cai et al., 2017) and Shift-Net (Yan et al., 2018). They adopt CNN structures to fill gaps by learning structural and textural information from images. However, like MPS methods, these CNN-based approaches typically require large amounts of complete image data as training samples, which are scarce in practice.

Self-supervised deep-learning methods have begun to receive attention recently to mitigate the requirement for labels (Kong et al., 2020; Liu et al., 2020, 2023; Saad et al., 2021; Fang et al., 2023; Li et al., 2024). These methods do not require complete image data as training samples; instead, they use the images' inherent structure and statistical properties to reconstruct missing or degraded formation images. For example, deep image prior (DIP) (Wang et al., 2019b) is a commonly used unsupervised deep-learning method that fills gaps in formation images by learning the prior distribution of images. However, DIP methods may introduce artifacts or over-smoothing without an appropriate early stop and, thus, require further refinement. Jiang et al. (2024) suggest a self-supervised approach to construct training data sets by further masking original images. Unlike DIP, these mask-based methods (Li et al., 2023b) reveal increased effectiveness as they learn from a broader spectrum of patterns. This underscores the importance of expansive training data sets. Accordingly, they are less effective than DIP at single-image filling with less pattern diversity.

In recent years, considerable interest has been shown in tensor-based representations. Tensor completion techniques, particularly low-rank tensor completion (Xie et al., 2018), have achieved success in various fields, such as seismic data interpolation (Liu et al., 2022), hyperspectral imaging reconstruction (Zhang et al., 2021), and traffic data prediction (Tan et al., 2013). Tensors, as extensions of matrices and vectors, better capture the intrinsic structure and relationships in multidimensional data (Zhang et al., 2022), thereby demonstrating powerful capabilities in recovering missing elements in incomplete multidimensional data. Compared with matrix completion techniques, tensor completion can better capture the high-order dependencies and structures in data, achieving higher recovery accuracy.

Introducing tensor-based methods in borehole imaging holds promise for addressing the challenge of recovering missing data and further unleashing the potential of borehole imaging technology. Because FMI images are obtained from observations of the same geologic structures, the pixels are highly correlated and exhibit low-order features. Therefore, using tensor-based methods to fill gaps in borehole images is feasible. By representing borehole imaging data in tensor form and applying techniques such as Tucker decomposition, we can better understand and use the latent structure and information in borehole data, achieving a more accurate and comprehensive description of formation features.

Among tensor decomposition methods, Tucker decomposition (Tucker, 1966) is a commonly used and powerful tool in various fields, such as image processing, signal analysis, and data compression, providing new insights and methods for data processing and analysis. It decomposes high-dimensional tensors into the product of multiple low-dimensional subspaces, thereby achieving efficient data representation and dimensionality reduction. Compared with higher-order singular value decomposition (HOSVD) (De Lathauwer et al., 2000), Tucker decomposition is particularly well suited for our application. Although both methods can decompose high-dimensional tensors into product forms, Tucker decomposition allows each mode to have its own dimensionality reduction matrix, which helps preserve the structural information of the data. In contrast, HOSVD requires the same dimensionality reduction matrix for all modes during reduction (Kolda and Bader, 2009), and its factor matrices are orthogonal, making HOSVD more suitable for applications that require orthogonal properties. In this work, we primarily use Tucker decomposition to capture the structure of our data. However, it is noteworthy that advanced decomposition techniques, such as tensor train (TT) (Zhang et al., 2022) and tensor ring (TR) (Sedighin and Cichocki, 2021), have been shown to achieve better performance than Tucker decomposition in traditional methods, especially in certain high-dimensional contexts (Oseledets, 2011). These techniques will be considered as potential avenues for future research to enhance our approach to high-dimensional problems.

Combining deep learning with tensor-based representations holds tremendous potential for advancing borehole imaging technology. Deep-learning techniques can learn features from large amounts of data, improving the model's generalization ability. Meanwhile, tensor-based representations can better capture the high-order relationships and structural information between data, especially for processing high-dimensional data. In recent years, fully connected TNNs have been widely applied to solve recovery problems, achieving remarkable results. For example, Liu et al. (2021) propose a fully connected tensor network decomposition method to effectively solve the robust tensor completion problem, achieving significant results. Zheng et al. (2021) demonstrate the application of fully connected tensor network decomposition in high-order tensor completion, further validating its superior performance. In addition, Yang et al. (2022) introduce a high-order tensor completion algorithm based on weighted optimization using fully connected tensor networks, showcasing excellent performance in practical applications. These studies indicate that fully connected TNNs exhibit great potential and advantages in fields such as image restoration and signal processing. By combining deep learning with tensor-based representations, we can fully exploit the advantages of deep learning in feature extraction and pattern recognition and the benefits of tensor representation in data representation and structural modeling, thereby improving the efficiency and accuracy of borehole image processing.

Inspired by this, we propose a self-supervised TNN with the robust representation capabilities of deep learning to enhance FMI image inpainting. The architecture of each network layer mirrors Tucker decomposition structure, allowing for self-supervised learning without fully labeled borehole images. This tensor computation forms the backbone of our model, which leverages the structural correlation inherent in geologic layers. Meanwhile, combining this with a deep network architecture improves the ability of the model to capture complex rock formations in detail. In addition, we integrate total variation (TV) regularization (Rudin et al., 1992) to ensure smoother filling effects of the reconstruction images. Because borehole images are originally in 2D, transforming them into tensor representations is a crucial step to harness the power of the proposed tensor representation. To this end, we propose an adaptive boundary-detection cropping with augmentation (ABDCA) algorithm to adapt 2D images into tensors. After data completion with the proposed method, we use adaptive slice concatenation with replacement (ASCR) to restore the enhanced images. This ensures that the tensor representation of 3D data is accurately shown in 2D images. Our research attempts to establish a new paradigm in borehole image filling, which can reliably operate amidst the challenges of scarce data and complex geologic structures. Validation using real-world data demonstrates the accuracy of the proposed approach. Combining deep learning with tensor representation enhances the model’s capacity to represent and reconstruct intricate patterns in borehole images, setting new benchmarks for high-accuracy reconstruction. The main contributions of this work can be summarized as follows:

- 1) We develop a self-supervised TNN aimed at enhancing FMI image restoration. The model leverages the inherent structural correlations within geologic layers, using tensor computation as a foundation and incorporating deep network architecture. This approach enables self-supervised learning without fully labeled borehole images. To the best of our knowledge, this is the first attempt at using the tensor method for borehole image interpolation.
- 2) To leverage the powerful reconstruction ability of tensorial networks, we propose an ABDCA algorithm to adapt 2D images into tensors. After processing the data using the proposed TNN method, we use ASCR to restore the enhanced images. This ensures that the tensor representation of 3D data is accurately shown in 2D images.
- 3) The proposed TNN framework can be enhanced by embedding a structural regularizer. This advancement is illustrated by incorporating TV regularization to ensure the continuity of the reconstructed image.

METHOD

Supervised deep learning has demonstrated remarkable proficiency in data reconstruction tasks. However, its success hinges on the availability of extensive, complete image data sets. This requirement often makes it impractical for borehole imaging because obtaining complete data sets is typically unfeasible with the current design of data collection tools. To address this challenge, we propose a self-supervised TNN based on Tucker decomposition (Balazević et al., 2019) to reduce dependence on complete image labels. Compared with conventional methods, the proposed model

not only effectively uses partial image information but also learns from the intrinsic features of the images to generate precise predicted results on image gaps. Through this approach, we can achieve effective filling of the borehole images even in the absence of complete image labels.

Generating tensor-based representation for borehole images

Tensors, as the higher-order extensions of matrices, are better at capturing multidimensional data structures and relationships (Zhang et al., 2022). FMI images, with their highly correlated pixels and low-rank characteristics, would benefit from tensor-based methods for filling gaps. To fully harness the multiway pixel correlations and spatial structural similarities within FMI images, we propose converting 2D borehole images into 3D tensors, enhancing the modeling of inherent correlations and structures.

In this paper, lowercase and uppercase bold letters (e.g., \mathbf{x} and \mathbf{X}) are used to denote vectors and matrices, and uppercase bold calligraphic letters (e.g., \mathcal{X}) represent higher-order tensors. For a tensor \mathcal{X} , $\mathbf{X}_{(p)}$ denotes the mode- p unfolding matrix of the tensor, and $\mathcal{X} \times_p \mathbf{A}$ represents the p -mode product of tensor \mathcal{X} with matrix \mathbf{A} . The notation “ \circ ” denotes the Hadamard product, $\|\cdot\|_F$ denotes the Frobenius norm, and \mathbf{A}^T represents the transpose of matrix \mathbf{A} . In addition, \mathbb{R} and \mathbb{C} are the real and complex fields.

We first illustrate our 3D tensor generation strategy with the example in Figure 1, which incorporates data augmentation, cropping, concatenation, and reversion. The original FMI borehole image, being cylindrical, is converted into 2D images by unwarping it from a chosen starting point. However, this starting point is selected arbitrarily, potentially leading to black borders that lose adjacent pixel information, complicating the interpolation. Notably, the 2D image is periodic, meaning these borders contain adjacent information mirrored on the opposite side. We augment the image by duplicating a section from the left side to the right to minimize boundary issues from unwarping. If the original image is $\mathbf{A}_0 \in \mathbb{R}^{M \times S}$, this process results in an image of $\mathbf{A} \in \mathbb{R}^{M \times N}$, where $N > S$.

Then, we segment the image into overlapping small patches of size $I \times J$ and sequentially stack them to form a 3D tensor $\mathcal{Y} \in \mathbb{R}^{I \times J \times K}$ in a left-to-right, top-to-bottom order. Figure 2a shows a standard cropping strategy with a fixed stride. However, closer inspection reveals that some patches have missing pixels exclusively on their outer edges, necessitating value estimation beyond the available data range, thus posing extrapolation challenges (Wang et al., 2019a). Extrapolation is inherently more complex than interpolation because it projects known data trends into uncharted territory, often without constraints, leading to potential error accumulation. We introduce an ABDCA method that addresses this by identifying boundary pixels during cropping and ensuring that unknown pixels are centered within the patches, as shown in Figure 2b. This strategy effectively mitigates extrapolation inaccuracies, which introduce errors at open-ended patch boundaries due to less context and compromise the fidelity of image generation. Consequently, avoiding extrapolation enhances the overall quality and accuracy of image synthesis. As shown in Figure 1, ABDCA adeptly traces the contours of missing gaps, enhancing the reliability of the reconstructed image by avoiding extrapolation. It is important to note that patches on the extreme left are exceptions; however, this is inconsequential as we have already augmented this data on the opposite side.

In the ABDCA method, we only need to set the initial size of small blocks manually. When a cropped small block has only one side containing known pixels, the algorithm automatically adjusts the block's position until both sides of the cropped block contain known pixels. Specifically, when the small block has known pixels only on the right side, the algorithm shifts the block's position to the left, and vice versa, ensuring that each side of the cropped block contains at least two columns of known pixels. If this condition is not fulfilled, a larger block size should be selected.

After completion, we convert the 3D data back into 2D images. We introduce the ASCR method, as shown in Figure 1. This method reverses the cropping process, reconstructing the patches into augmented 2D data. Building on the ABDCA method, which augments images to preserve the boundary continuity, ASCR selectively replaces this section to revert the filled data to their original 2D form. This careful restoration ensures that the tensor representation of 3D data is accurately reflected in the resulting 2D images.

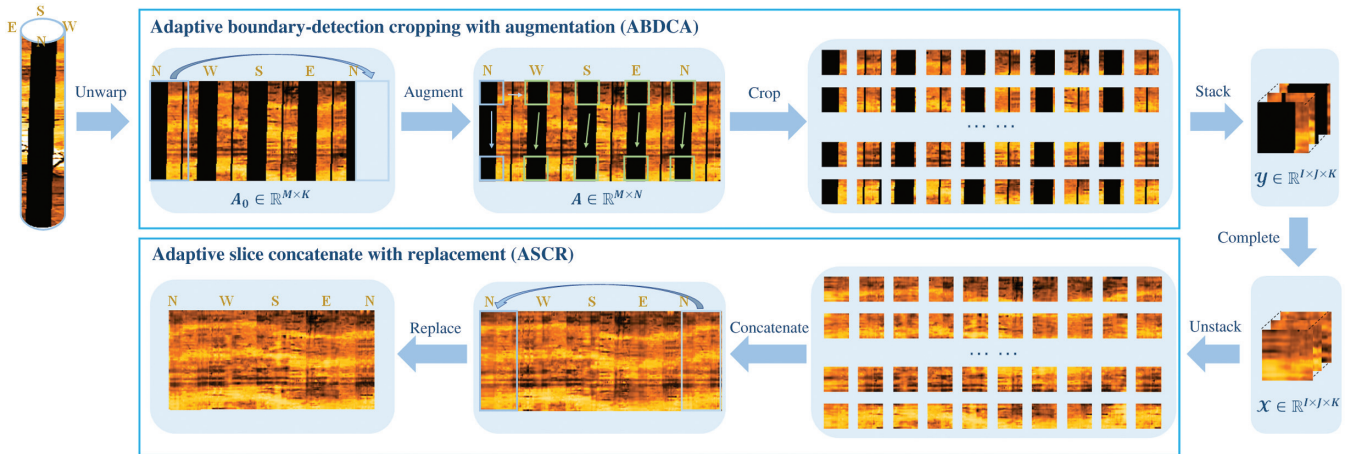


Figure 1. Workflow for filling image gaps with tensor representation. FMI data are initially unwarped to create a 2D image. This image is then processed using the ABDCA method to form a tensor representation. Upon completion, the 3D tensor data are converted back into a 2D image through the ASCR method.

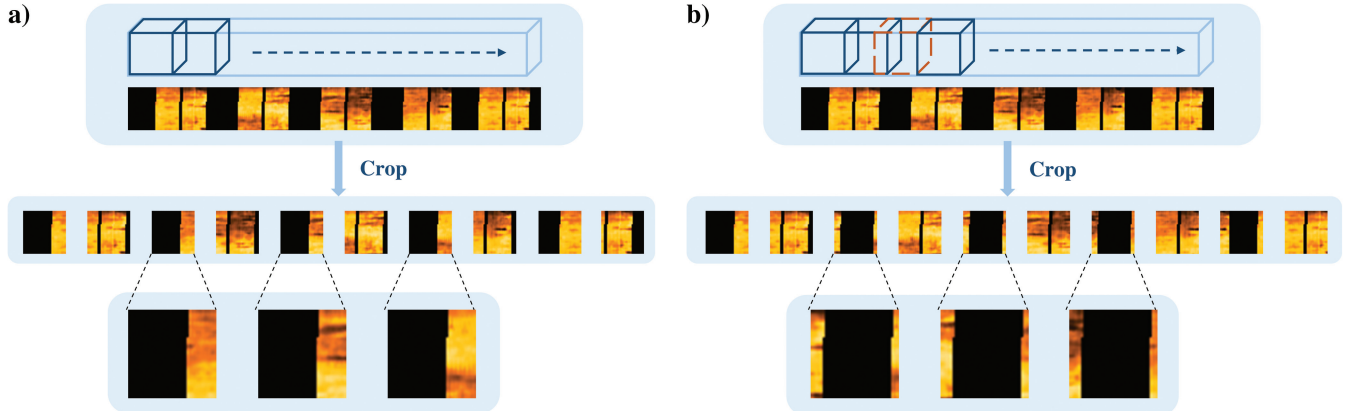


Figure 2. A comparison of different cropping strategies. (a) Standard cropping with a fixed stride, wherein some patches have missing pixels exclusively on their outer edges, and (b) the adaptive boundary-detection cropping. We repetitively slice a portion of the known pixels from the original data to ensure that both sides of the cropped patches contain the known data, thereby avoiding challenging extrapolation and improving the reliability of the filled image.

Formulation of the tensor reconstruction problem

This section introduces the fundamental formulation of 3D tensor completion. Let us consider an observed 3D tensor $\mathcal{Y} \in \mathbb{R}^{I \times J \times K}$, which contains elements that are either known or missing. The complete data, without any missing elements, are denoted by $\mathcal{X} \in \mathbb{R}^{I \times J \times K}$. Their relationship can be expressed as

$$\mathcal{Y} = \mathcal{O} \circ \mathcal{X}, \quad (1)$$

where “ \circ ” signifies the Hadamard product and \mathcal{O} is a binary sampling operator defined as follows:

$$\mathcal{O}_{(i,j,k)} = \begin{cases} 0 & \text{if } \mathcal{Y}(i,j,k) \text{ is a missing entry} \\ 1 & \text{if } \mathcal{Y}(i,j,k) \text{ is an observed entry} \end{cases}. \quad (2)$$

Suppose one wants to recover the missing entries of \mathcal{Y} . In that case, it is essential to leverage prior knowledge about the complete tensor \mathcal{X} . Typically, tensor completion methods presuppose that \mathcal{X}

exhibits certain structural properties, such as the ability to be closely approximated through decompositions, such as Tucker (Yokota et al., 2018), TT, or TR. This implies that \mathcal{X} can be represented as $\mathcal{D}(\vartheta)$, where ϑ denotes the decomposition parameters or latent factors. If we use a model to approximate \mathcal{X} , the relationship can be expressed as

$$\mathcal{X} = \mathcal{D}(\vartheta). \quad (3)$$

The tensor reconstruction problem can thus be formulated as an optimization task expressed as

$$\min_{\vartheta} \|\mathcal{Y} - \mathcal{O} \circ \mathcal{D}(\vartheta)\|_F^2. \quad (4)$$

This reformulation enables the use of the observed \mathcal{Y} to estimate the model's optimal parameters ϑ^* , intending to minimize the Frobenius norm of the difference between the observed tensor and the Hadamard product of \mathcal{O} with the approximated tensor $\mathcal{D}(\vartheta)$. Using the learned model parameter ϑ^* , the 3D tensor is reconstructed by $\mathcal{D}(\vartheta^*)$.

TNN-aided image completion algorithm

In recent years, deep neural networks (DNNs) have seen extensive application in various fields, such as computer vision (He et al., 2022), acoustic signal processing (Ozanich et al., 2020; Wolf et al., 2020; Hua et al., 2023), and data reconstruction (Li et al., 2023a). Known for their feature extraction capabilities, DNNs excel at learning complex nonlinear representations. Coupling DNNs with tensor representation has sparked significant interest, as it promises to capture the inherent structure of multidimensional data better. In this context, we enhance tensor representation by postulating that 3D tensors can be effectively represented within an L -layer neural network, which can be mathematically formulated as

$$\mathcal{X} = \mathcal{D}(\vartheta) = F_{\theta_L}(F_{\theta_{L-1}}(\cdots F_{\theta_1}(\mathcal{G}))), \quad (5)$$

where $F_{\theta_L}(\cdot)$ represents the L th layer function with parameters θ_i , and \mathcal{G} represents the core tensor. To comply with the notation of

equation 4, ϑ encompasses the set of all parameters, such as \mathcal{G} and $\{\theta_i\}_{i=1}^L$. Building on a DNN representation model, our goal is to reconstruct the 3D tensor by solving the following optimization problem:

$$\min_{\vartheta} \|\mathcal{Y} - \mathcal{O} \circ F_{\theta_L}(F_{\theta_{L-1}}(\cdots F_{\theta_1}(\mathcal{G})))\|_F^2, \quad (6)$$

where we aim to determine the optimal parameter set ϑ^* that minimizes the discrepancy between the observed data \mathcal{Y} and the reconstructed data, thus addressing the missing data problem effectively.

Given the scarcity of complete borehole images for training, solving equation 6 is tricky for supervised learning. To effectively solve the challenge of borehole image completion without constructing training labels, a highly expressive model is required to capture the intricate spatial distribution details. Drawing inspiration from recent advances in tensor-based data completion and the powerful feature extraction capabilities of DNN, we extract the best of both worlds to address the inherent challenges of limited borehole image data availability. We propose a self-supervised TNN for borehole image completion. As shown in Figure 3, this approach uses Tucker decomposition method, renowned for its effectiveness with high-dimensional data, to design a network architecture. Each layer is modeled after Tucker decomposition structure. This facilitates self-supervised learning by encoding prior knowledge of low-rank structural correlations into the network architecture. Multiple layers of this type harness the full potential of tensor-based models to capture the inherent correlation between pixels within geologic features.

We update the network parameters by minimizing the loss function in equation 6, which evaluates the output image only at the known pixel locations in the original borehole image. The generated 3D tensor \mathcal{Y} is the learning target for the model. To enable self-supervision, we configure the input \mathcal{G} as a down-sampled version of \mathcal{Y} obtained through bilinear interpolation, directing the network to generate complete images. The design of the network allows the use of simple gradient descent algorithms, ensuring good results from limited samples. After estimating ϑ^* , the network can reasonably fill in the initial gaps in borehole images and generate complete images without any discernible artifacts. In addition, we integrate TV regularization to enhance the continuity of the filling results,

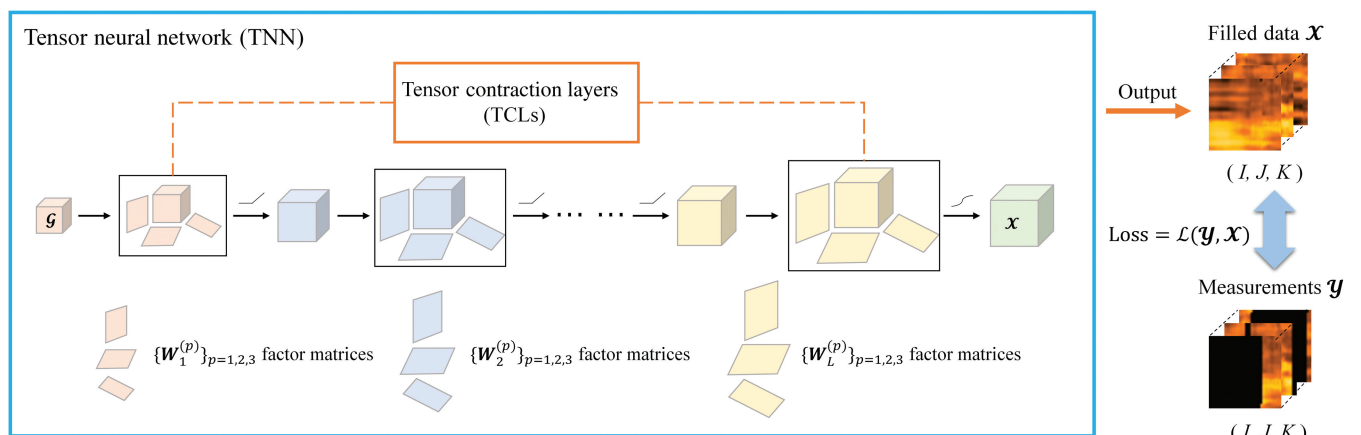


Figure 3. The TNN architecture for borehole image completion. The 3D tensor \mathcal{Y} , constructed by ABDCA, serves as the learning target. The input \mathcal{G} is the core tensor, and we designated it as the downsampled \mathcal{Y} after bilinear interpolation. After network training, the output yields the filled borehole \mathcal{X} . Similar to the conventional Tucker decomposition, the input \mathcal{G} and factor matrices $\{\mathbf{W}^{(p)}\}_{p=1}^3$ are learnable parameters for successful image completion.

enabling the TNN network to reconstruct the intricate features of borehole images accurately.

Integrating Tucker decomposition and neural network for FMI image representation

Our study introduces a TNN combining tensor decomposition with the robust representational abilities of DNNs to enhance FMI image filling. At the heart of our lightweight model are tensor computations, which capitalize on the structural correlations within geologic layers. Concurrently, incorporating DNN architecture boosts the model's capability to detail the intricacies of rock formations.

Drawing on Tucker decomposition model (Balažević et al., 2019), we can theoretically approximate a 3D tensor using tensors as follows:

$$\mathcal{X} \approx \mathcal{S} \times_1 \mathbf{U}^{(1)} \times_2 \mathbf{U}^{(2)} \times_3 \mathbf{U}^{(3)}, \quad (7)$$

where the columns of factor matrices $\{\mathbf{U}^{(p)}\}_{p=1,2,3}$ serve as spatial basis functions, and the core tensor \mathcal{S} comprises weighting coefficients. This representation is valuable for extracting meaningful patterns, such as subtle variations and structural information in 3D tensors, with efficient storage and faster computations.

Inspired by this, we develop a tensor contraction layer (TCL) (Kossaifi et al., 2020), as shown in Figure 4. TCL takes an input tensor $\mathcal{X}_l \in \mathbb{R}^{R_1^l \times R_2^l \times R_3^l}$ and produces an output through

$$\mathcal{X}_{l+1} = \varsigma(\mathcal{X}_l \times_1 \mathbf{W}_l^{(1)} \times_2 \mathbf{W}_l^{(2)} \times_3 \mathbf{W}_l^{(3)}), \quad (8)$$

where the output tensor is $\mathcal{X}_{l+1} \in \mathbb{R}^{R_1^{l+1} \times R_2^{l+1} \times R_3^{l+1}}$ ($R_m^{l+1} > R_m^l, m = 1, 2, 3$). The factor matrix is represented by $\mathbf{W}_l^{(i)} \in \mathbb{R}^{R_i^{l+1} \times R_i^l}$, and $\varsigma(\bullet)$ is an activation function. Taking advantage of Tucker decomposition, TCL exhibits high expressiveness and conciseness, capturing multidimensional correlations in 3D data with minimal trainable parameters.

Stacking multiple TCLs together forms the proposed TNN network in Figure 3. Mathematically, this layering can be described as

$$\begin{aligned} \mathcal{X}_{\text{TNN}} = \mathcal{D}(\vartheta) = \varsigma_L(\cdots \varsigma_1(\mathcal{G} \times_1 \mathbf{W}_{11} \times_2 \mathbf{W}_{12} \times_3 \mathbf{W}_{13}) \cdots \\ \times_1 \mathbf{W}_{L1} \times_2 \mathbf{W}_{L2} \times_3 \mathbf{W}_{L3}), \end{aligned} \quad (9)$$

where the core tensor $\mathcal{G} \in \mathbb{R}^{R_1 \times R_2 \times R_3}$, $\{\mathbf{W}_l^{(i)}\}_{i=1}^3$ are factor matrices for all layers, and L is the total number of layers. These TCLs transform the input tensor \mathcal{G} into the output tensor \mathcal{X} through sequential

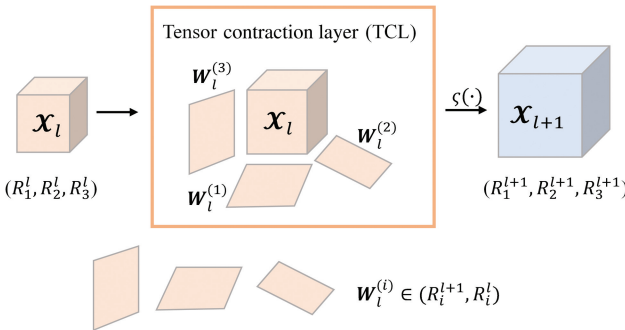


Figure 4. Illustration of single-layer TCLs, where \mathcal{X}_l is the input, \mathcal{X}_{l+1} is the output, $\{\mathbf{W}_l^{(p)}\}_{p=1}^3$ is the factor matrices, and $\varsigma(\bullet)$ is the activation function.

tensor contraction operations coupled with a nonlinear activation function $\varsigma_l(\cdot)$ after each layer l . The activation function selection is tailored to the data, with common choices being the rectified linear unit, sigmoid, and tanh (Karlik and Olgac, 2011). Accordingly, the proposed TNN network can effectively capture both linear and nonlinear features across multiple dimensions, leading to better-filled borehole images.

TNN-aided reconstruction algorithm

Regularization terms integrate additional prior information, thereby boosting performance. Based on the proposed TNN model, we incorporate an extra regularization term, and inserting equation 9 into equation 6 yields the following optimization problem for borehole image reconstruction:

$$\min_{\vartheta} \|\mathcal{Y} - \mathcal{O} \circ \mathcal{X}_{\text{TNN}}\|_F^2 + \lambda R(\mathcal{X}_{\text{TNN}}), \quad (10)$$

where $\vartheta = \{\mathcal{G}, \mathbf{W}_l^{(1)}, \mathbf{W}_l^{(2)}, \mathbf{W}_l^{(3)}\}_{l=1}^L$ denotes the set of trainable parameters, $R(\mathcal{X})$ signifies a regularization term, and λ is a hyper-parameter that balances data fitting and the regularization term. If $\lambda = 0$, the regularization term becomes ineffective, reverting to the original formula in equation 6. Choosing different regularization terms can incorporate various types of prior structural information. In this study, we adopt a classic anisotropic TV regularization (Rudin et al., 1992) represented by

$$\begin{aligned} R(\mathcal{X}) = \sum_{i,j,k} (|\mathcal{X}_{i+1,j,k} - \mathcal{X}_{i,j,k}| + |\mathcal{X}_{i,j+1,k} - \mathcal{X}_{i,j,k}| \\ + |\mathcal{X}_{i,j,k+1} - \mathcal{X}_{i,j,k}|). \end{aligned} \quad (11)$$

Gradient descent, a fundamental first-order optimization method, is widely used in training networks due to its straightforwardness. The model parameters set $\vartheta = \{\mathcal{G}, \mathbf{W}_l^{(1)}, \mathbf{W}_l^{(2)}, \mathbf{W}_l^{(3)}\}_{l=1}^L$ and is updated using the gradient descent method (Nesterov, 2013), with the update rule

$$\vartheta_{k+1} = \vartheta_k - g_k \nabla_{\vartheta} f(\vartheta_k), \quad (12)$$

where ϑ_k and ϑ_{k+1} are the model parameters at iterations k and $k+1$, respectively, and g_k is the corresponding learning rate. Advanced optimization techniques such as adaptive gradient algorithm, root-mean-squared propagation, and Adam are recom-

Algorithm 1: TNN-aided borehole image completion algorithm.

Input: The generated tensor $\mathcal{Y} \in \mathbb{R}^{I \times J \times K}$, the core tensor $\mathcal{G} \in \mathbb{R}^{R_1 \times R_2 \times R_3}$, the mask tensor $\mathcal{O} \in \mathbb{R}^{I \times J \times K}$, and the iteration number K .

Parameter: λ, g_k

Output: Reconstruction \mathcal{X}

- 1: **Initialize:** $k = 0, \vartheta$
- 2: **while** $k < K$ **do**
- 3: Calculate the gradients $\nabla_{\vartheta} f(\vartheta_k)$
- 4: Update ϑ via $\vartheta_{k+1} \leftarrow g_k \nabla_{\vartheta} f(\vartheta_k)$
- 5: $k = k + 1$
- 6: **end while**
- 7: **Return** $\mathcal{X} = \mathcal{D}(\vartheta_K)$

mended. These methods, especially effective for large data sets (Fan et al., 2014), can further enhance algorithmic performance (Ruder, 2016). We summarize the proposed algorithm in Algorithm 1. Although the core tensor \mathcal{G} serves as the algorithm's input, it remains a trainable model parameter. In addition, the factor matrices $\{\mathbf{W}_l^{(1)}, \mathbf{W}_l^{(2)}, \mathbf{W}_l^{(3)}\}_{l=1}^L$ mentioned previously are model training parameters and are not inputs to the algorithm.

RESULTS

In this section, we present the results obtained with field drilling images for gap filling, intending to highlight the exceptional performance of the proposed TNN in addressing gap-filling tasks. We conducted multiple experiments covering various conditions, such as scenarios with and without real ground data, experiments with and without preinputting core tensors, and interpolation experiments on large fractures. In addition, we conducted a comparative analysis of our method with three state-of-the-art deep-learning approaches, fully connected tensor decomposition and tensor completion (FCTN-TC), (Zheng et al., 2021), DIP (Ulyanov et al., 2018), and deep generative prior (DGP) (Pan et al., 2021).

Experimental settings

In this section, we applied the TNN network to fill in the gaps in the drilling images. Before training, we used the ABDCA method mentioned previously to expand the image $\mathbf{A}_0 \in \mathbb{R}^{160 \times 313}$, transforming it into an image $\mathbf{A} \in \mathbb{R}^{160 \times 400}$, and then performed adaptive cropping to generate the 3D tensor $\mathcal{Y} \in \mathbb{R}^{40 \times 40 \times 40}$.

We input the preprocessed 3D tensor $\mathcal{Y} \in \mathbb{R}^{40 \times 40 \times 40}$ into the TNN network to obtain complete 3D drilling data $\mathcal{X} \in \mathbb{R}^{40 \times 40 \times 40}$. Then, we applied the ASCR method mentioned previously to convert the 3D data into 2D data, thus obtaining the complete drilling image. To demonstrate the feasibility of the TNN network on scarce data, we selected a typical on-site example. As shown in Figure 5a, it mainly consists of parallel sandstone layers.

Due to the lack of ground-truth data in the measured FMI images and to obtain a more robust quantitative comparison of the different methods, we initially filled the small gaps in the resistivity images using bilinear interpolation, as shown in Figure 5b, to serve as the ground-truth data. Subsequently, a portion of the image was designated as invisible, as shown in Figure 5c, to serve as the input data for evaluating the filling performance.

The filling performance of the different methods is evaluated using the root-mean-square error (RMSE), defined by the formula:

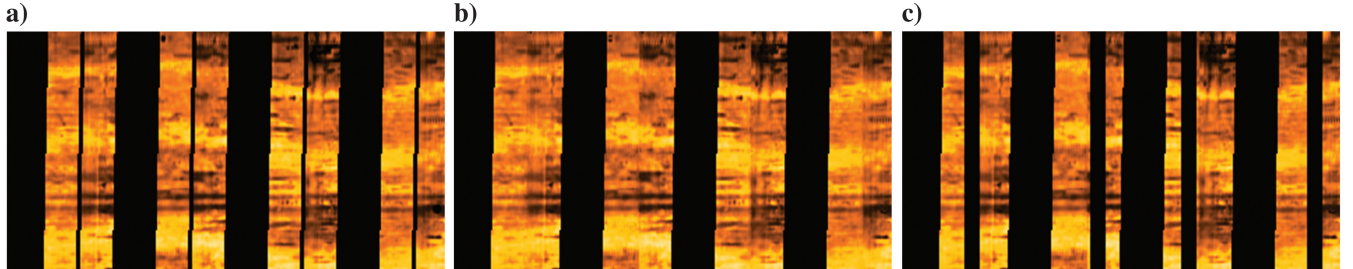


Figure 5. (a) A typical field image with gaps, primarily consisting of parallel sandstone layers, (b) ground-truth data are obtained by filling small gaps using bilinear interpolation, and (c) input data are obtained by decimating the former ground-truth data. These manually removed regions are used for comparison. All images have a size of 160 by 313 pixels, with a depth discretization of 2.54 mm (0.1 in.) per pixel and an azimuthal discretization of 1.125° per pixel.

$$\text{RMSE} = \sqrt{\frac{1}{T} \sum_{i=1}^I \sum_{j=1}^J \sum_{k=1}^K (\mathcal{X}_{ijk} - \tilde{\mathcal{X}}_{ijk})^2}, \quad (13)$$

where \mathcal{X} represents the ground-truth data, $\tilde{\mathcal{X}}$ is the filled data, and $T = I \times J \times K$ represents the total number of data points.

The algorithm used TensorFlow's automatic differentiation mechanism for gradient computation. To optimize the proposed TNN model, specifically, we used the Adam optimizer for model optimization, setting the learning rate to 0.005 and performing 15,000 iterations.

Comparison of different TNN depths

To assess recoverability and gain a better understanding of the proposed model, we designed three different configurations of the TNN models (as shown in Table 1). These models were trained and tested separately for scenarios with and without designating the inputting core tensors. It is important to note that for models without core tensor inputs, the core tensors are randomly generated. In contrast, for models with core tensor inputs, the core tensors are derived by downsampling the original 3D data to the corresponding size using maximum pooling. The results are shown in Figure 6.

The results show that all three TNN networks demonstrate satisfactory filling performances. In the absence of core tensors, quantitative calculations indicate that the RMSE values for the three TNN networks are 0.0197, 0.0210, and 0.0236, respectively. This suggests that deeper networks perform better in filling images when core tensors are not specified from the downsampled \mathcal{Y} . This improvement can be attributed to the greater number of parameters in deeper networks, allowing the model to fill the data more effectively. By increasing the network depth, the model can learn more complex image features, thereby enhancing filling performance.

Table 1. Different configurations of the TNN models.

Method	Number of layers in TNN	Dimensionality
TNN1	4	(5,5,5) (10,10,10) (20,20,20) (40,40,40)
TNN2	3	(10,10,10) (20,20,20) (40,40,40)
TNN3	2	(20,20,20) (40,40,40)

When the core tensor is provided, deeper TNN networks perform slightly better, with RMSE values of 0.0183, 0.0198, and 0.0231. The improved filling performance, compared with the same networks without the core tensor, is evident from the lower RMSE

Table 2. Comparison of BRISQUE scores for different TNN models.

Type	Core	Without core
TNN1	29.2538	30.1256
TNN2	30.1562	31.1263
TNN3	31.5416	32.5674

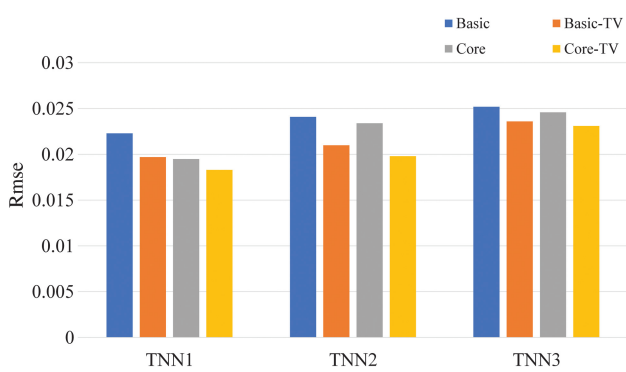


Figure 6. The filling results of different TNN methods. The “Basic” method does not have a preinput core tensor, and its core tensor is randomly generated. In contrast, the “Core” method’s core tensor is derived from the downsampled \mathcal{Y} .

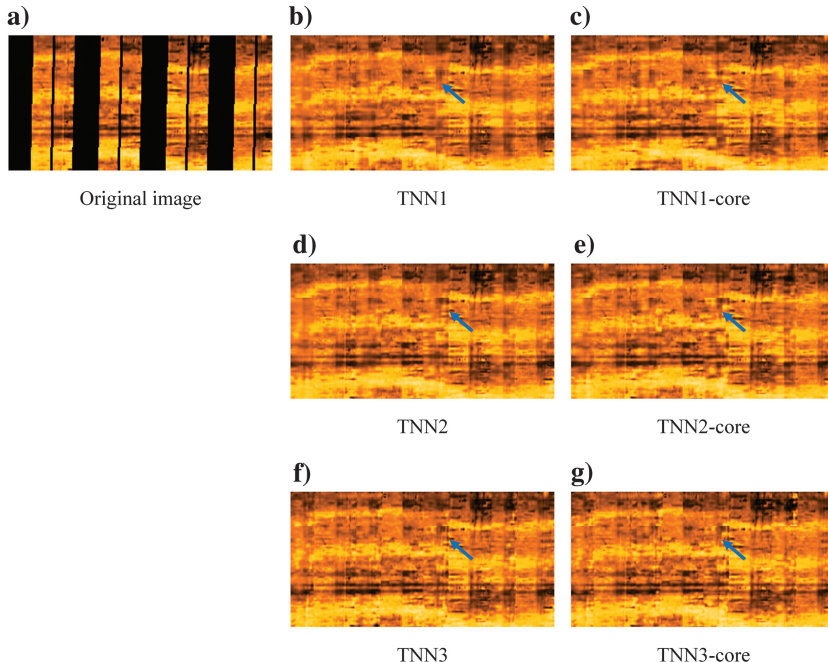


Figure 7. The filling results of different TNN methods. (a) The original image, (b–d) filling results without inputting the core tensor, and (e–g) filling results by inputting the core tensor. As indicated by the blue arrows, the TNN1-core method performs better in restoring the details. All images have a size of 160 by 313 pixels, with a depth discretization of 2.54 mm (0.1 in.) per pixel and an azimuthal discretization of 1.125° per pixel.

values. This finding confirms the superior filling performance of the TNN networks with the core tensor. The input of core tensors helps the network better capture the data features, enhancing the accuracy and consistency of image inpainting and demonstrating their importance in complex image processing tasks.

Without using TV regularization, the network performance declines, regardless of whether core tensors are provided. This result clearly highlights the crucial role of TV regularization in maintaining and enhancing network performance. Specifically, TV regularization improves network performance by suppressing noise and preserving the overall structure of the image, demonstrating its value in processing borehole image data.

The preceding experiments demonstrate that generating core tensors and using TV regularization can better guide the reconstruction process, producing more accurate and reliable results. Indeed, this observation underscores the critical role of using existing information to improve the accuracy and consistency of the interpolation process, thereby enhancing the final results.

Next, we applied the aforementioned TNN1-core methods to fill in the unknown pixels, and the results are shown in Figure 7. The results demonstrate that these methods effectively recover the missing regions. In addition, the TNN1-core still stands out for its remarkable recovery performance. The image filled by the TNN1-core retains the essential geologic features and textures effectively and exhibits high visual quality, as indicated by the blue arrows. Furthermore, good preservation of lateral consistency with the surrounding known features is observed. This observation aligns with our previous conclusions, further validating the superiority of the TNN1-core method in filling unknown pixels.

To provide a more comprehensive comparison, we used the blind/referenceless image spatial quality evaluator (BRISQUE) (Mittal et al., 2012)

metric to quantitatively assess the filling capabilities of the models, as shown in Table 2. BRISQUE is a no-reference image quality assessment method that effectively measures the quality of an image. The evaluation results using this metric revealed that, consistent with previous conclusions, the TNN1-core method demonstrates superior performance in filling unknown pixels. Specifically, the BRISQUE metric indicates that the TNN1 method excels in handling complex image structures and detail restoration. This further validates the reliability and effectiveness of the TNN1-core method, proving its potential and practical value in enhancing image filling quality.

Comparison of different deep-learning methods

To comprehensively evaluate our method, we conducted quantitative comparisons with three other methods: FCTN-TC (Zheng et al., 2021), DIP (Ulyanov et al., 2018), and DGP (Pan et al., 2021). To ensure fair comparisons, we preprocessed and normalized the input images for the DIP and DGP methods, uniformly resizing them to 256 × 256 normalized images. During this process, we set the number of iterations for DIP to 6000 and used a publicly available

pretrained model for DGP, maintaining the initial restoration configuration. Similarly, we cropped and concatenated the same images into 4D data as the input for FCTN-TC, using the publicly available FCTN-TC model and maintaining the initial recovery configuration. For our method, we selected TNN1-core as a representative of our method for comparative analysis.

To visually compare the filling effects, we present the filling results of images with ground-truth data for the four methods on two different structures, as shown in Figures 8 and 9. Although the DIP method produces relatively smooth images, it significantly lacks detail, appearing overly blurry. The DGP and FCTN-TC show structures in detail but exhibit inaccuracies, which diminish the overall image quality. As indicated by the red boxes, the FCTN-TC, DIP, and DGP methods produce inaccurate results and are less effective in recovering details compared with the TNN method.

In comparison, the TNN method exhibits superior performance across various aspects. First, the TNN method not only retains more image details but also produces more reliable filling results with lower distortion. In addition, the TNN method demonstrates higher accuracy in handling complex image structures, ensuring a high degree of consistency between the filled areas and the surrounding known regions. These observations further validate the superiority of the TNN method in the image-filling process, excelling in reducing errors and maintaining the integrity of image structures.

To provide a more objective and comprehensive evaluation, we introduced multiple evaluation metrics, such as structural similarity index (SSIM), peak signal-to-noise ratio (PSNR), mean-squared error (MSE), and computational time. Compared with the previous comparison based solely on RMSE, adopting multiple metrics allows for a more thorough assessment of each method's strengths and weaknesses across different aspects, thus yielding a more accurate reflection of their actual performance. Table 3 shows the comparison results of these metrics. It is noteworthy that our method outperforms the FCTN-TC, DGP, and DIP methods across all metrics, demonstrating its superiority.

For example, in terms of SSIM, our method shows greater similarity, indicating excellent performance in maintaining image structure integrity. Regarding PSNR, our method achieves higher values, suggesting better performance in noise suppression and signal fidelity. The reduction in MSE also highlights our method's superiority in minimizing image errors. Furthermore, our method is the most efficient method in terms of processing time. Notably, we evaluated these metrics only within the masked regions filled by the methods to ensure the accuracy and comparability of the evaluation results. This comparison provides a comprehensive assessment of our method's performance, thoroughly validating its effectiveness.

Then, we applied the aforementioned methods to fill in the unknown pixels. By feeding the input images into the four methods, we obtained the fill-

ing images from the different methods, as shown in Figure 10. When handling images with simple sinusoidal structures, all four methods performed adequately in filling. However, in terms of detail, the FCTN-TC and DGP methods introduced noticeable noise, as indicated by the blue arrows, whereas regions generated by the DIP method lacked significant detailed features, failing to recover clear textures. The differences among the methods became more pronounced when dealing with more complex structures, as indicated

Table 3. The evaluation metrics of different methods.

Type	TNN	FCTN-TC	DIP	DGP
SSIM↑	0.9519	0.9015	0.9312	0.8459
PSNR↑	18.2985	16.1561	15.4524	12.4515
MSE↓	0.0148	0.0346	0.0285	0.0571
TIME↓	23 s	354 s	278 s	299 s

Upward arrow indicates that higher value is better, while downward arrow indicates that lower value is better.

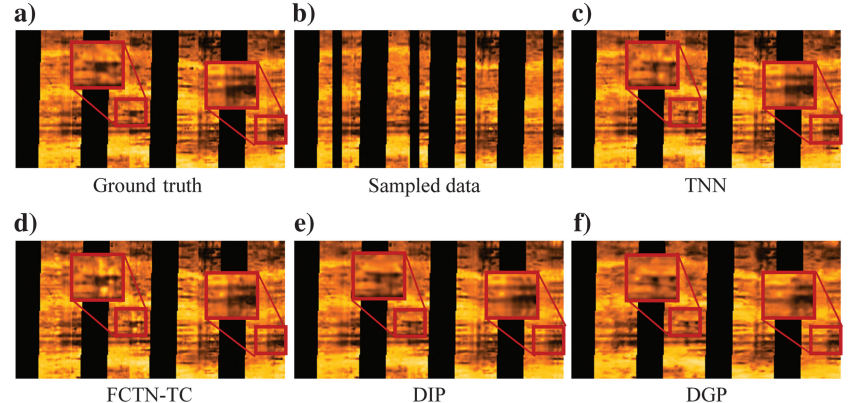


Figure 8. The filling results of different methods. (a) The ground-truth data, (b) sampled data, (c) TNN, (d) FCTN-TC, (e) DIP, and (f) DGP. As indicated by the red boxes, the FCTN-TC, DIP, and DGP methods produce inaccurate results and are less effective in recovering the details compared with the TNN method.

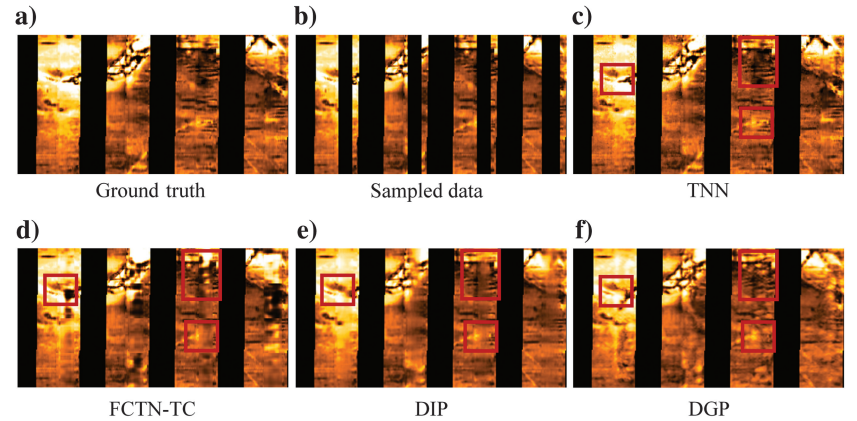


Figure 9. The filling results of different methods. (a) The ground-truth data, (b) sampled data, (c) TNN, (d) FCTN-TC, (e) DIP, and (f) DGP. As indicated by the red boxes, the FCTN-TC, DIP, and DGP methods produce inaccurate results and are less effective in recovering the details compared with the TNN method.

by the red boxes. FCTN-TC showed significant discrepancies from the original image data, resulting in inaccurate filling. Although the regions generated by the DIP method were smooth, they also lacked detailed features, struggling to restore texture details within complex structures. The DGP method performed poorly in recovering the sinusoidal structures of the images, failing to maintain the desired lateral consistency. In contrast, our method demonstrated significant advantages in all aspects. Our method efficiently restored reasonable and detailed features while maintaining satisfactory lateral consistency with the surrounding known features, resulting in more realistic filling results.

To better compare the filling effects of the different methods, we used the BRISQUE metric for the quantitative assessment of the models' filling capabilities, as shown in Table 4. The evaluation results were consistent with our previous conclusions, further validating the superiority of the TNN method in filling unknown pixels. Specifically, the BRISQUE metric indicated that the TNN method outperformed the other methods across all evaluation metrics, highlighting its advantages in maintaining image structure integrity and detail restoration. Through a quantitative evaluation using the BRISQUE metric, we obtained a more comprehensive and objective comparison of the filling effects of different methods. This comprehensive evaluation method provided clear data support, enabling us to more accurately understand the superiority of the TNN method in handling complex image filling tasks. The results demonstrate that the TNN method not only excels in visual effects but also outperforms the FCTN-TC, DIP, and DGP methods across multiple technical metrics.

Table 4. Comparison of BRISQUE scores for different methods.

Data	TNN	FCTN-TC	DIP	DGP
I↓	35.2656	40.4997	37.2513	40.5752
II↓	28.9500	31.4227	32.2309	34.6354
III↓	29.2538	31.2935	32.2819	39.5199

Downward arrow indicates that a lower value is better.

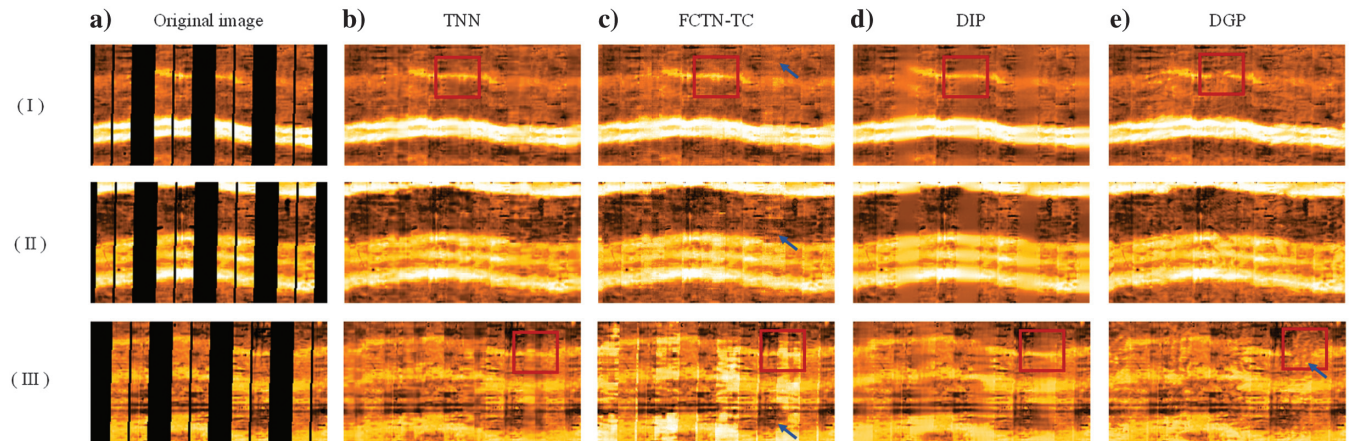


Figure 10. The filling results of different methods on three different structures. (a) The original image, (b) TNN, (c) FCTN-TC, (d) DIP, and (e) DGP. The DGP method introduces discontinuities in the sinusoidal structures, as highlighted by the red boxes. Similarly, the FCTN-TC method also exhibits discontinuities in the sinusoidal structures, particularly in the subpart labeled III. In addition, the DIP method causes blurring of the details. The blue arrows indicate the noise generated by the FCTN-TC and DGP methods.

Filling large fractures with different deep-learning methods

In the final stage of the experiment, we tested the ability of the TNN method to fill in visible high-angle fractures, as shown in Figure 11. These large fractures may result from changes in underground pressure, tectonic movements, or other geologic activities causing rock layer breakage. Filling large-angle fractures is crucial for geologic exploration. Using the same experimental parameters as previously, we divided the selected 480×313 image with large fractures into three equal parts vertically. After processing these parts with the ABDCA method, they were transformed into three tensors of size (40,40,40) and individually input into the network. Finally, they were concatenated together using the ASCR method. The application of four different methods to fill the large fracture areas produced impressive results. Consistent with previous comparisons, the filling effect of the DIP method appeared overly smooth, lacking a distinct presentation of detailed features, as shown in the red boxes. In contrast, although the FCTN-TC and DGP methods performed reasonably well in filling large fractures, they still exhibited limitations. For instance, DGP struggled with maintaining good connectivity in handling large fractures, whereas the FCTN-TC method could introduce some noise, as indicated by the blue arrows, which affects the filling quality. In comparison, our method was able to restore reasonable and detailed features while maintaining lateral consistency with the surrounding known features.

To further validate our findings, we introduced the BRISQUE metric for comparison, as shown in Table 5. The BRISQUE scores reaffirmed our previous conclusions, further validating the superior performance of the TNN method in filling large fractures.

Table 5. Comparison of BRISQUE scores for filling large fracture images using different methods.

Type	TNN	FCTN-TC	DIP	DGP
BRISQUE↓	32.2372	35.5407	35.6940	36.8455

Downward arrow indicates that a lower value is better.

The filled images demonstrate the excellent performance of the TNN method in handling complex geologic structures and successfully restoring the geologic features and texture details around the large crack. Meanwhile, the filled images exhibit more coherent and realistic geologic structures, maintaining good consistency with the surrounding known areas. This result further validates the TNN method's practicality and effectiveness in drilling image filling. By showcasing the outstanding performance of the TNN method in filling large cracks, we aim to provide deeper insights into the immense potential of this method in solving real-world problems, offering more inspiration and opportunities for the development of the geologic image processing field.

DISCUSSION

Why are high-order pixel correlations important?

To compare the impact of the 3D tensors versus the 2D data inputs on filling performance, we attempted to directly input the 2D data into the network, as shown in Figure 12. The restoration performance of the pure 2D blocks was inferior to that of the 3D data, as shown in the red boxes, likely because 3D data enhance the ability to use spatial correlations. Our findings indicate that interpolating 3D tensors is necessary and effective in our study. This underscores the importance and effectiveness of interpolating 3D tensors in complex image processing tasks.

Limitations and future work

Although the TNN method has shown promising results in filling borehole images, it still has several limitations. First, although the TNN method can fill in the missing parts of an image, it struggles when the missing areas are large. Due to the reduction in known pixels, the completion ability of the TNN networks will decrease. Specifically, when the missing region exceeds the network's capacity, the remaining known pixel information is insufficient to support accurate reconstruction, leading to unsatisfactory filling results.

To further explore this issue, we introduced additional gaps into the original borehole images. These gaps varied in size: 5 pixels, 10 pixels, and 15 pixels, as shown in Figure 13. Through experimentation, we observed a gradual decrease in the effectiveness of image restoration as these newly introduced gap sizes increased. This suggests that the size of the missing areas significantly influences the outcome of the image restoration; larger gaps make the restoration process more challenging, thereby leading to poorer recovery outcomes.

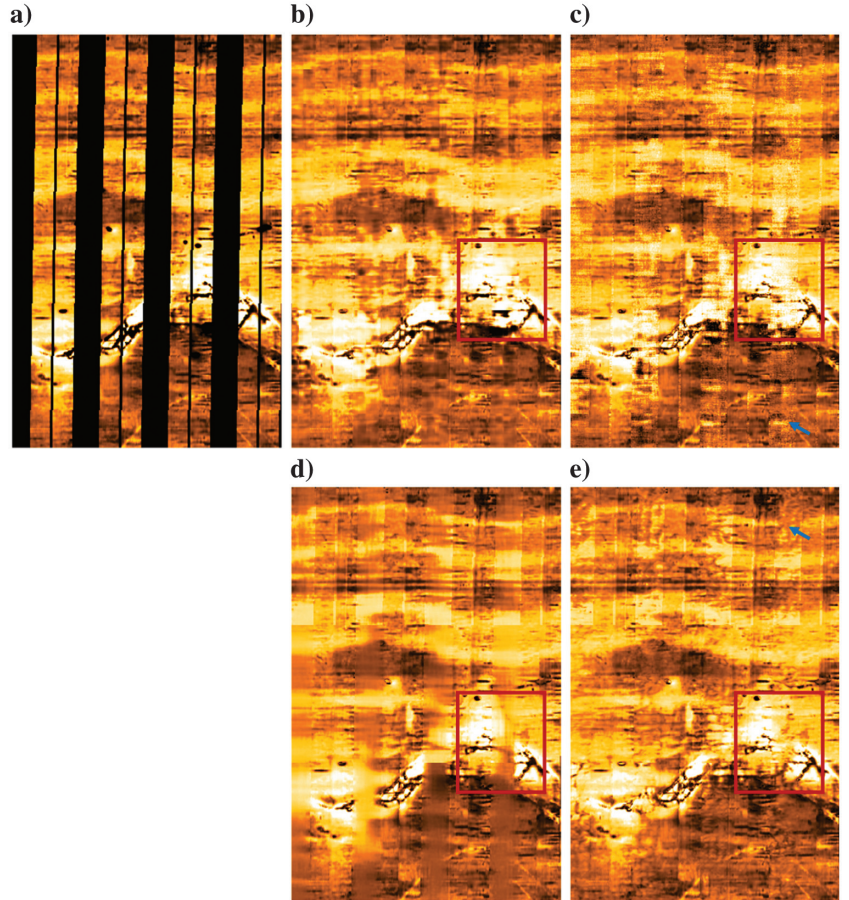


Figure 11. The result of filling large fractures using different methods. (a) The original image, (b) TNN, (c) FCTN-TC, (d) DIP, and (e) DGP. The red boxes highlight our superior performance in detail preservation, whereas the other methods blur these structures. The blue arrows indicate the noise introduced by the FCTN-TC and DGP methods. All images have a size of 480 by 313 pixels, with a depth discretization of 2.54 mm (0.1 in.) per pixel and an azimuthal discretization of 1.125° per pixel.

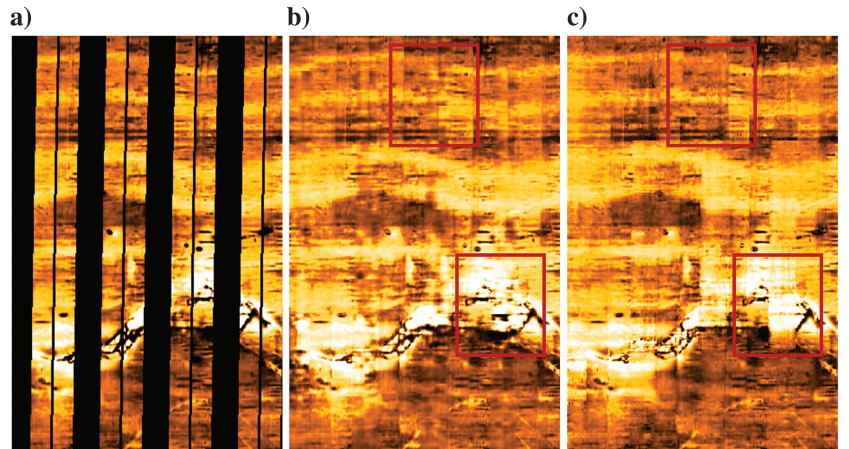


Figure 12. Interpolation results obtained from TNN with different input data on large fracture images. (a) The original image, (b) interpolation results obtained by the TNN method with 3D tensor input, and (c) interpolation results obtained by the TNN method with 2D input. The red box highlights how our method recovers more details by exploiting high-order structural information.

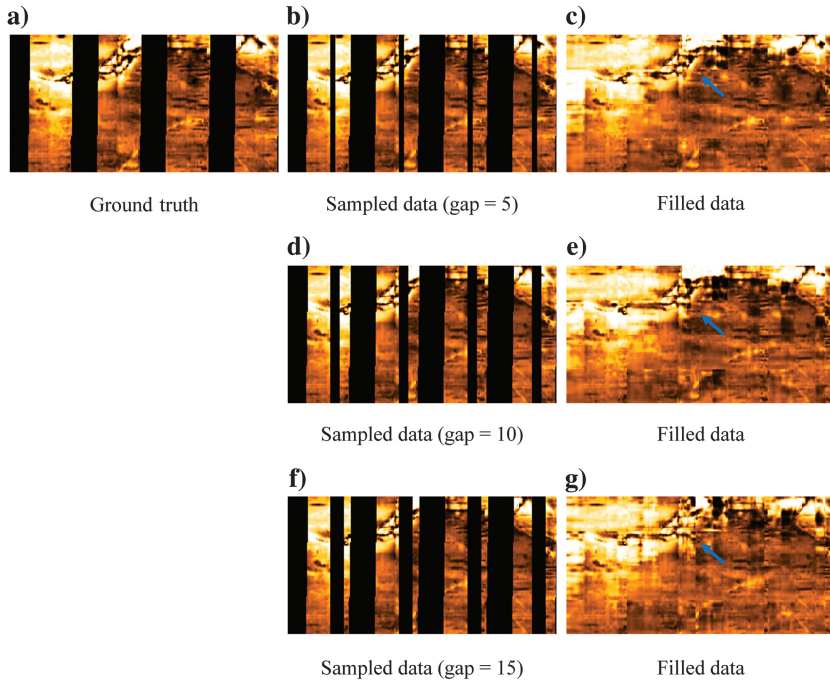


Figure 13. The results of filling different gaps: (a) the original data; (b, d, and f) the data sampled with gaps of 5, 10, and 15 pixels, respectively; and (c, e, and g) the data after filling by the TNN method for gaps of 5, 10, and 15 pixels, respectively. The blue arrows indicate the differences in filling results for different gap sizes.

The second limitation is that all previous TNN methods used input data of fixed size (40,40,40) obtained by the ABDCA method. This data structure can maintain the TNN network's performance to some extent. However, when we attempt to use larger 3D data, the TNN network fails to achieve the same high-quality results. We suspect this is because as the data size increases, its low-rank property changes, resulting in decreased performance when handling high-dimensional data. This indicates that in order to effectively handle larger data sets, more complex tensor structures or more detailed parameter adjustments are needed. Future work might explore implementing TT (Oseledets, 2011) or TR networks (Zhao et al., 2016; Wang et al., 2018) to enhance our model's capabilities.

The third point is that FMI images inherently have a 40% data loss. Although the ABDCA method can effectively avoid extrapolation, it falls short when the missing areas in the middle of the FMI images are larger. This may reduce the accuracy and reliability of image filling. Therefore, for FMI images with large missing areas, the existing TNN and ABDCA methods may require advanced pre-processing to handle these complex situations better.

Despite the TNN method demonstrating good performance in borehole image filling, further research and improvement are needed to address the previously mentioned limitations, thereby enhancing its performance and adaptability for large-scale applications.

CONCLUSION

We have introduced a novel framework for borehole image inpainting using a self-supervised TNN based on Tucker decomposition. Our approach reduces dependency on fully annotated images, effectively filling image gaps even with limited training data. By

leveraging tensor-based representations and DNNs combined with anisotropic TV regularization, we achieve accurate reconstruction of complex features in borehole images. Experimental results demonstrate the effectiveness of our method in generating complete images without significant artifacts, promising advancements in borehole imaging and contributing to a better understanding of underground geologic structures.

Although Tucker decomposition was the most suitable approach for this study, we recognize that TT and TR decompositions have demonstrated greater effectiveness in traditional decomposition scenarios, particularly for handling higher-dimensional tensors. These methods present promising directions for future research, as they could enhance adaptability and computational efficiency when dealing with even larger data sets. Although we know these alternative methods for tensor representation, our focus in this paper is on applying a single method — Tucker decomposition — to address a practical geophysical problem. We intended not to compare Tucker decomposition with the range of available methods in the literature for decomposing multilinear arrays but to highlight the practicality of the adopted decomposition in this specific context.

ACKNOWLEDGMENTS

This work was supported in part by the National Natural Science Foundation of China under grant 42374135, in part by the National Key Research and Development Program of China under grant 2021YFA0716903, and in part by the Fundamental Research Funds for the Central Universities under grant xzy012023073. The contribution of the first author was supported by the industrial sponsors of the Signal Analysis and Imaging Group (SAIG) consortium at the University of Alberta.

DATA AND MATERIALS AVAILABILITY

Data associated with this research are available and can be obtained by contacting the corresponding author.

REFERENCES

- Assous, S., P. Elkington, and J. Whetton, 2014, Microresistivity borehole image inpainting: *Geophysics*, **79**, no. 2, D31–D39, doi: [10.1190/geo2013-0188.1](https://doi.org/10.1190/geo2013-0188.1).
- Balažević, I., C. Allen, and T. M. Hospedales, 2019, TuckER: Tensor factorization for knowledge graph completion: arXiv preprint, doi: [10.48550/arXiv.1901.09590](https://arxiv.org/abs/1901.09590).
- Cai, N., Z. Su, Z. Lin, H. Wang, Z. Yang, and B. W.-K. Ling, 2017, Blind inpainting using the fully convolutional neural network: *The Visual Computer*, **33**, 249–261, doi: [10.1007/s00371-015-1190-z](https://doi.org/10.1007/s00371-015-1190-z).
- De Lathauwer, L., B. De Moor, and J. Vandewalle, 2000, A multilinear singular value decomposition: *SIAM Journal on Matrix Analysis and Applications*, **21**, 1253–1278, doi: [10.1137/S0895479896305696](https://doi.org/10.1137/S0895479896305696).
- Fan, J., F. Han, and H. Liu, 2014, Challenges of big data analysis: *National Science Review*, **1**, 293–314, doi: [10.1093/nsr/nw1032](https://doi.org/10.1093/nsr/nw1032).
- Fang, W., L. Fu, M. Wu, J. Yue, and H. Li, 2023, Irregularly sampled seismic data interpolation with self-supervised learning: *Geophysics*, **88**, no. 3, V175–V185, doi: [10.1190/geo2022-0586.1](https://doi.org/10.1190/geo2022-0586.1).

- He, K., X. Chen, S. Xie, Y. Li, P. Dollár, and R. Girshick, 2022, Masked autoencoders are scalable vision learners: Proceedings of the IEEE/CVF Conference on Computer Vision and Pattern Recognition, 16000–16009.
- Hua, X., L. Cheng, T. Zhang, and J. Li, 2023, Interpretable deep dictionary learning for sound speed profiles with uncertainties: The Journal of the Acoustical Society of America, **153**, 877–894, doi: [10.1121/10.0017099](https://doi.org/10.1121/10.0017099).
- Hurley, N. F., and T. Zhang, 2011, Method to generate full-bore images using borehole images and multipoint statistics: SPE Reservoir Evaluation & Engineering, **14**, 204–214, doi: [10.2118/120671-PA](https://doi.org/10.2118/120671-PA).
- Jiang, L., X. Si, and X. Wu, 2024, Filling borehole image gaps with a partial convolution neural network: Geophysics, **89**, no. 2, D89–D98, doi: [10.1190/geo2022-0344.1](https://doi.org/10.1190/geo2022-0344.1).
- Karlik, B., and A. V. Olgac, 2011, Performance analysis of various activation functions in generalized MLP architectures of neural networks: International Journal of Artificial Intelligence and Expert Systems, **1**, 111–122.
- Kolda, T. G., and B. W. Bader, 2009, Tensor decompositions and applications: SIAM Review, **51**, 455–500, doi: [10.1137/07070111X](https://doi.org/10.1137/07070111X).
- Kong, F., P. Picetti, V. Lipari, P. Bestagini, X. Tang, and S. Tubaro, 2020, Deep prior-based unsupervised reconstruction of irregularly sampled seismic data: IEEE Geoscience and Remote Sensing Letters, **19**, 1–5, doi: [10.1109/LGRS.2020.3044455](https://doi.org/10.1109/LGRS.2020.3044455).
- Kossaifi, J., Z. C. Lipton, A. Kolbeinsson, A. Khanna, T. Furlanello, and A. Anand-Kumar, 2020, Tensor regression networks: Journal of Machine Learning Research, **21**, 1–21.
- Li, J., D. Liu, D. Trad, and M. Sacchi, 2024, Robust unsupervised 5D seismic data reconstruction on both regular and irregular grid: Geophysics, **89**, no. 6, V537–V549, doi: [10.1190/geo2024-0098.1](https://doi.org/10.1190/geo2024-0098.1).
- Li, S., L. Cheng, T. Zhang, H. Zhao, and J. Li, 2023a, Striking the right balance: Three-dimensional ocean sound speed field reconstruction using tensor neural networks: The Journal of the Acoustical Society of America, **154**, 1106–1123, doi: [10.1121/10.0020670](https://doi.org/10.1121/10.0020670).
- Li, S., L. Zhang, Z. Wang, D. Wu, L. Wu, Z. Liu, J. Xia, C. Tan, Y. Liu, B. Sun, and S. Li, 2023b, Masked modeling for self-supervised representation learning on vision and beyond: arXiv preprint, doi: [10.48550/arXiv.2401.00897](https://doi.org/10.48550/arXiv.2401.00897).
- Liu, D., Z. Deng, C. Wang, X. Wang, and W. Chen, 2020, An unsupervised deep learning method for denoising prestack random noise: IEEE Geoscience and Remote Sensing Letters, **19**, 1–5, doi: [10.1109/LGRS.2020.3019400](https://doi.org/10.1109/LGRS.2020.3019400).
- Liu, D., M. D. Sacchi, and W. Chen, 2022, Efficient tensor completion methods for 5-D seismic data reconstruction: Low-rank tensor train and tensor ring: IEEE Transactions on Geoscience and Remote Sensing, **60**, 1–17, doi: [10.1109/TGRS.2022.3179275](https://doi.org/10.1109/TGRS.2022.3179275).
- Liu, D., M. D. Sacchi, X. Wang, and W. Chen, 2023, Unsupervised deep learning for ground roll and scattered noise attenuation: IEEE Transactions on Geoscience and Remote Sensing, **19**, 1–5, doi: [10.1109/TGRS.2023.3325324](https://doi.org/10.1109/TGRS.2023.3325324).
- Liú, Y.-Y., X.-L. Zhao, G.-J. Song, Y.-B. Zheng, and T.-Z. Huang, 2021, Fully-connected tensor network decomposition for robust tensor completion problem: arXiv preprint, doi: [10.48550/arXiv.2110.08754](https://doi.org/10.48550/arXiv.2110.08754).
- Loftis, J., and L. Bourke, 1999, The recognition of artefacts from acoustic and resistivity borehole imaging devices: Geological Society, London, Special Publications, **159**, 59–76.
- Luthi, S., 2001, Geological well logs: Their use in reservoir modeling: Springer Science & Business Media.
- Mariethoz, G., and P. Renard, 2010, Reconstruction of incomplete data sets or images using direct sampling: Mathematical Geosciences, **42**, 245–268, doi: [10.1007/s11004-010-9270-0](https://doi.org/10.1007/s11004-010-9270-0).
- Mittal, A., R. Soundararajan, and A. C. Bovik, 2012, Making a “completely blind” image quality analyzer: IEEE Signal Processing Letters, **20**, 209–212, doi: [10.1109/LSP.2012.2227726](https://doi.org/10.1109/LSP.2012.2227726).
- Mustapha, H., and R. Dimitrakopoulos, 2010, High-order stochastic simulation of complex spatially distributed natural phenomena: Mathematical Geosciences, **42**, 457–485, doi: [10.1007/s11004-010-9291-8](https://doi.org/10.1007/s11004-010-9291-8).
- Nesterov, Y., 2013, Introductory lectures on convex optimization: A basic course: Springer Science & Business Media, volume 87.
- Oseledets, I. V., 2011, Tensor-train decomposition: SIAM Journal on Scientific Computing, **33**, 2295–2317, doi: [10.1137/090752286](https://doi.org/10.1137/090752286).
- Ozanich, E., P. Gerstoft, and H. Niu, 2020, A feedforward neural network for direction-of-arrival estimation: The Journal of the Acoustical Society of America, **147**, 2035–2048, doi: [10.1121/10.0000944](https://doi.org/10.1121/10.0000944).
- Pan, X., X. Zhan, B. Dai, D. Lin, C. C. Loy, and P. Luo, 2021, Exploiting deep generative prior for versatile image restoration and manipulation: IEEE Transactions on Pattern Analysis and Machine Intelligence, **44**, 7474–7489, doi: [10.1109/TPAMI.2021.3115428](https://doi.org/10.1109/TPAMI.2021.3115428).
- Rider, M. H., 1986, The geological interpretation of well logs: Blackie.
- Ruder, S., 2016, An overview of gradient descent optimization algorithms: arXiv preprint, doi: [10.48550/arXiv.1609.04747](https://doi.org/10.48550/arXiv.1609.04747).
- Rudin, L. I., S. Osher, and E. Fatemi, 1992, Nonlinear total variation based noise removal algorithms: Physica D: Nonlinear Phenomena, **60**, 259–268, doi: [10.1016/0167-2789\(92\)90242-F](https://doi.org/10.1016/0167-2789(92)90242-F).
- Saad, O. M., Y. A. S. I. Oboue, M. Bai, L. Samy, L. Yang, and Y. Chen, 2021, Self-attention deep image prior network for unsupervised 3-D seismic data enhancement: IEEE Transactions on Geoscience and Remote Sensing, **60**, 1–14, doi: [10.1109/TGRS.2021.3108515](https://doi.org/10.1109/TGRS.2021.3108515).
- Sedighin, F., and A. Cichocki, 2021, Image completion in embedded space using multistage tensor ring decomposition: Frontiers in Artificial Intelligence, **4**, 687176, doi: [10.3389/frai.2021.687176](https://doi.org/10.3389/frai.2021.687176).
- Tan, H., G. Feng, J. Feng, W. Wang, Y.-J. Zhang, and F. Li, 2013, A tensor-based method for missing traffic data completion: Transportation Research Part C: Emerging Technologies, **28**, 15–27, doi: [10.1016/j.trc.2012.12.007](https://doi.org/10.1016/j.trc.2012.12.007).
- Tucker, L. R., 1966, Some mathematical notes on three-mode factor analysis: Psychometrika, **31**, 279–311, doi: [10.1007/BF02289464](https://doi.org/10.1007/BF02289464).
- Ulyanov, D., A. Vedaldi, and V. Lempitsky, 2018, Deep image prior: Proceedings of the IEEE Conference on Computer Vision and Pattern Recognition, 9446–9454.
- Wang, W., Y. Sun, B. Eriksson, W. Wang, and V. Aggarwal, 2018, Wide compression: Tensor ring nets: Proceedings of the IEEE Conference on Computer Vision and Pattern Recognition, 9329–9338.
- Wang, Y., X. Tao, X. Shen, and J. Jia, 2019a, Wide-context semantic image extrapolation: Proceedings of the IEEE/CVF Conference on Computer Vision and Pattern Recognition, 1399–1408.
- Wang, Z., N. Gao, R. Zeng, X. Du, X. Du, and S. Chen, 2019b, A gaps filling method for electrical logging images based on a deep learning model: Well Logging Technology, **43**, 578–582.
- Wolf, T., L. Debut, V. Sanh, J. Chaumond, C. Delangue, A. Moi, P. Cistac, T. Rault, R. Louf, M. Funtowicz, and J. Davison, 2020, Transformers: State-of-the-art natural language processing: Proceedings of the 2020 Conference on Empirical Methods in Natural Language Processing: System Demonstrations, 38–45.
- Xie, T., S. Li, L. Fang, and L. Liu, 2018, Tensor completion via nonlocal low-rank regularization: IEEE Transactions on Cybernetics, **49**, 2344–2354, doi: [10.1109/TCYB.2018.2825598](https://doi.org/10.1109/TCYB.2018.2825598).
- Yan, Z., X. Li, M. Li, W. Zuo, and S. Shan, 2018, Shift-Net: Image inpainting via deep feature rearrangement: Proceedings of the European Conference on Computer Vision, 1–17.
- Yang, P., Y. Huang, Y. Qiu, W. Sun, and G. Zhou, 2022, A high-order tensor completion algorithm based on fully-connected tensor network weighted optimization: Chinese Conference on Pattern Recognition and Computer Vision, 411–422.
- Yokota, T., B. Erem, S. Guler, S. K. Warfield, and H. Hontani, 2018, Missing slice recovery for tensors using a low-rank model in embedded space: Proceedings of the IEEE Conference on Computer Vision and Pattern Recognition, 8251–8259.
- Zhang, S., L. Wang, L. Zhang, and H. Huang, 2021, Learning tensor low-rank prior for hyperspectral image reconstruction: Proceedings of the IEEE/CVF Conference on Computer Vision and Pattern Recognition, 12006–12015.
- Zhang, T., P. Switzer, and A. Journel, 2006, Filter-based classification of training image patterns for spatial simulation: Mathematical Geology, **38**, 63–80, doi: [10.1007/s11004-005-9004-x](https://doi.org/10.1007/s11004-005-9004-x).
- Zhang, Y., Y. Wang, Z. Han, and Y. Tang, 2022, Effective tensor completion via element-wise weighted low-rank tensor train with overlapping ket augmentation: IEEE Transactions on Circuits and Systems for Video Technology, **32**, 7286–7300, doi: [10.1109/TCSVT.2022.3181471](https://doi.org/10.1109/TCSVT.2022.3181471).
- Zhao, Q., G. Zhou, S. Xie, L. Zhang, and A. Cichocki, 2016, Tensor ring decomposition: arXiv preprint, doi: [10.48550/arXiv.1606.05535](https://doi.org/10.48550/arXiv.1606.05535).
- Zheng, Y.-B., T.-Z. Huang, X.-L. Zhao, Q. Zhao, and T.-X. Jiang, 2021, Fully-connected tensor network decomposition and its application to higher-order tensor completion: Proceedings of the AAAI Conference on Artificial Intelligence, 11071–11078.

Biographies and photographs of the authors are not available.